Forward modelling of D camera view in ST40 informed by experimental data

Forward modelling of D_α camera view in ST40 informed by experimental data

A. Aimetta[a], M. Moscheni[b], L. Singh[a], C. Marsden[b], A. Scarabosio[c], M. Sertoli[b], A. Sladkomedova[b], F. Subba[a], J. Varje[b], H. Wu[a]

[a] *NEMO Group, Dipartimento Energia, Politecnico di Torino, Corso Duca degli Abruzzi 24, 10129, Torino, Italy,*
[b] *Tokamak Energy Ltd., 173 Brook Drive, Milton Park, Abingdon, United Kingdom,*
[c] *LINKS Foundation, Via Pier Carlo Boggio 61, Torino, 10138, Italy,*

Abstract

Embedding diagnostics in future pilot plants will be a challenging task, because of space- and irradiation-related concerns. Relying on high-fidelity synthetic diagnostics would then be valuable.

The 3D Monte-Carlo ray-tracing code CHERAB allows the development of numerous synthetic spectroscopic diagnostics. Focus of the present work is the introduction of new CHERAB models. The forward modelling of a synthetic D_α camera in ST40, the privately funded, high-field spherical tokamak, owned and operated by Tokamak Energy Ltd, and the comparison against experimental data is chosen as a testbed for quality assessment. Main output of the study then consists of estimates of the neutral particle densities throughout the chamber, of crucial relevance within edge plasma studies.

Starting from simple analytical models, a 2D D_α source in the poloidal plane is generated. However, the centre column limited plasmas in ST40 display an intrinsically-3D D_α emission, mostly localised around the discrete poloidal limiters on the centre column, not captured by any axisymmetric source model. Hence, a novel methodology is introduced in CHERAB to approximate the 3D non-toroidally-symmetric pattern via a piece-wise emission distribution.

Irrespective of the geometry of the emission and size of the tokamak, the pronounced non-homogeneity in the edge plasma emission requires sub-millimetric ($\sim$ power fall-off length) spatial resolution to guarantee an accurate estimate of the peak emission. Minimising the associated burden via implementation of a non-uniform source sampling algorithm, which is a modification of the standard CHERAB uniform sampling, results in a >10-fold reduction of the computational cost.

The significantly-shortened simulation time also makes the inclusion of more sophisticated models affordable. Of potential appeal in view of highly-detached divertors, the approximation of optically thin plasma is dropped, and photon-plasma interactions are accounted for. Brand-new CHERAB models able to take into account phenomena of photon absorption and scattering are so introduced.

Keywords: Synthetic diagnostic, D_α radiation, Spherical tokamak, Raysect, Cherab

Email address: alex.aimetta@polito.it (A. Aimetta)

1. Introduction

In the next generation of nuclear fusion devices, a significantly increased plasma performance with respect to existing tokamaks is aimed at being achieved and sustained for pilot-plant-relevant timescales. Such a mission requires plasma properties and power and particle exhaust to be reliably quantified during the design phase, and ultimately diagnosed during operations to build the basis for relevant code validation and extrapolation to pilot plants.

Pilot plants, with the aim of proving the feasibility of electricity production from nuclear fusion, will soon populate the landscape also. In such devices, the neutron irradiation would reach levels never experienced before and become of primary concern from the viewpoints of operation and servicing. The diagnostic apparatus would thus struggle to properly operate in, and even to survive *in primis*, this harsh environment [1].

It is in this framework that synthetic diagnostics become a tool of appeal to the fusion community. On the one hand, synthetic diagnostics offer support within the experimental data interpretation, of well-known peculiarly-challenging nature. On the other hand, synthetic diagnostics allow for a careful diagnostic design and integrated analyses devoted to fast capturing the essential plasma features [2]. The D_α camera is one such example: by allowing to infer properties of the neutral deuterium distribution throughout the chamber, this tool becomes of interest, e.g., in diagnosing the edge plasma, especially in regimes of detached divertor.

In this work we employ the 3D Monte-Carlo inverse ray-tracing code CHERAB [3][4] to model the 2D view of a synthetic D_α camera in the ST40 tokamak [5], the privately funded, high-field spherical tokamak, owned and operated by Tokamak Energy Ltd. With the ultimate goal of inferring valuable neutral parameters, focus is also put on the improvement of the existing numerical tools and methods in view of later systematic applications.

To this extent, the D_α emission source is built via simplified analytical models for the core and edge plasma as consistently as possible with the experimental data, as discussed in Sec. 2. Instead, Sec. 3 highlights the new CHERAB models developed. A new CHERAB model qualitatively capturing the substantial lack of toroidal symmetry of the ST40 centre column is introduced in Sec. 3.1. Then, a novel implementation of a non-uniform sampling algorithm in CHERAB aimed at reducing the computational burden of spatially resolving the dishomogeneous edge plasma radiation emission is discussed in Sec. 3.2. Last, Sec. 3.3 details the process of replacing the approximation of optically thin plasma with the implementation of photon absorption and scattering, of potential interest in pilot-plant-relevant detached plasmas. The results of the work, with comparison of the different models and assessment of the overall sensitivity to the input parameters, are discussed in Sec. 4, while Sec. 5 summarises the conclusions and outlook of the paper.

2. Experimental data and analytical source

2.1. Experimental data

Time instant 65 ms within plasma shot #9229 in the ST40 database is selected for the present analysis because of: (i) the satisfactory plasma current of 490 kA, the central ion and electron temperature of ~ 5.3 keV and ~ 2.5 keV, respectively, and the central electron density approaching $\sim 2.6 \times 10^{19}$ m^{-3}; (ii) the thorough investigations conducted by

the ST40 Team. These make such discharge an appropriate testbed for the new CHERAB models presented in this paper. The corresponding EFIT-reconstructed magnetic equilibrium [6] and experimental D_α camera view are shown in Fig. 1 and Fig. 2.a, respectively, while a schematic of the view in the toroidal plane (R, ϕ) is given in Fig. 3. The plasma is limited to the centre column and the D_α emission (lux) is hence localised on the $N_{\mathrm{LIM}} = 8$ discrete poloidal limiters (4 visible in Fig. 2.a), each of $\Delta\phi_{\mathrm{LIM}} = 0.23$ rad (= 13 degrees) in width along the toroidal direction ϕ.
Further noteworthy features of the experimental view are:

- The up-down asymmetry in the radiation emission, which is preferentially localised in the lower half of the centre column. Reason of this is ascribed to the asymmetry in the magnetic coil setup, reverberating in an asymmetry in the equilibrium (see, e.g., magenta separatrix in Fig. 1).

- The sigmoid pattern along the vertical direction Z, visible upon the two central limiters. As suggested by field-line tracing computations (Fig. 2.b), the surface struck by the plasma (where most of the D_α emission is localised) must indeed be the left (right) half of the limiters for $Z < 0$ ($Z > 0$). This is due to the interplay between magnetic shadowing and the direction of the magnetic field lines - impinging on the limiters from right to left (left to right) for $Z < 0$ ($Z > 0$).

- The non-zero emission from the vicinity of the passive plates (top and bottom extremities of the centre column) caused by a fraction of power and particles actually striking the passive plates rather than the limiters.

The plasma wetting affecting only the half-width of the limiters is taken into account in Sec. 3.1. On the contrary, believed to give minor corrections to the overall result, the remaining features are not included in the present analysis.

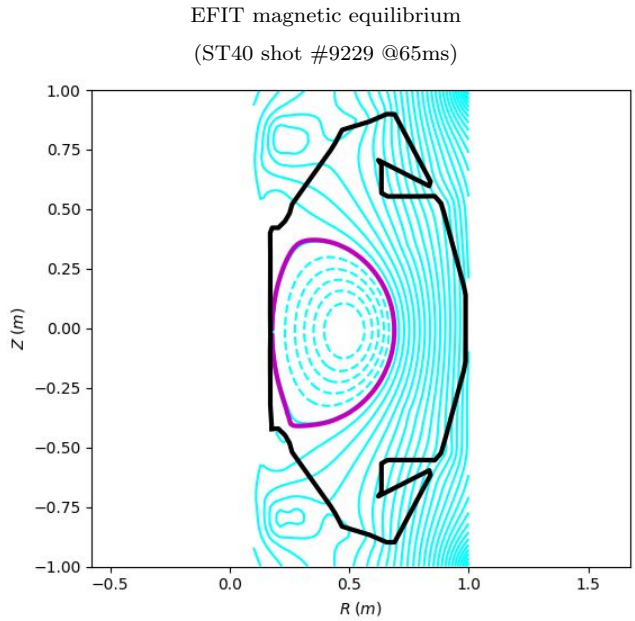

Figure 1: EFIT-reconstructed magnetic equilibrium [6] (cyan) of the plasma shot #9229 at 65 ms and separatrix (magenta). Dashed field lines belong to the plasma core region, while solid ones to the edge.

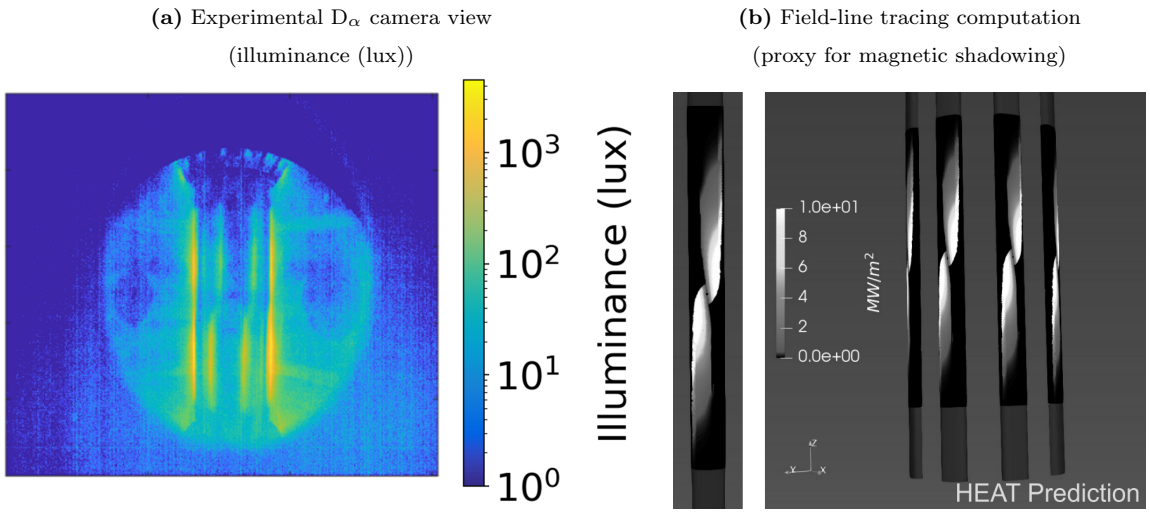

Figure 2: (a) D_α camera experimental view of the plasma shot #9229 at 65 ms. (b) Pattern of advective and conductive plasma heat flux (proxy for magnetic shadowing) on the ST40 limiters (right) computed via field-line tracing with the HEAT code [7]. Detail of one only limiter on the left. Black regions are magnetically shadowed in the optical approximation. Courtesy of [8].

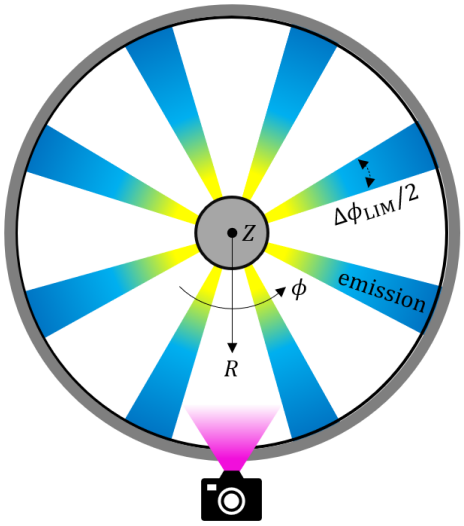

Figure 3: Cartoon of the top-view (toroidal plane) of the emission distribution (Sec. 3.1) enclosed by the ST40 wall (black and grey), with the reference frame adopted, $N_{\mathrm{LIM}} = 8$ and $\Delta\phi_{\mathrm{LIM}} \sim 13$ degrees (as per ST40 specs). While no emission is assumed to occur within the white volumes, D_α photons isotropically originate from the complementary emitting regions (yellow = high emission, blue = low emission) and propagate throughout the chamber. At the bottom, the position of the actual camera and its field of view (magenta).

2.2. Analytical source

Plasma profiles of density and temperature (Sec. 2.2.1), and neutral density (Sec. 2.2.2) are required to compute the corresponding D_α radiation emission (Sec. 2.2.3). Relying upon profiles obtained via core and edge plasma simulations as in [9] would hinder the possibility of several subsequent adjustments of the distribution itself, because of the substantial computational cost of the underlying plasma simulations. On the other hand, core plasma profiles computed via hierarchical data analysis (HDA) are available [2]. Nonetheless, both the associated uncertainty in the near-separatrix region and the sensitivity of the outcome to very near-separatrix figures (Sec. 4.2) make using HDA profiles unsuitable in the present context. For these reasons, analytical models are employed instead.

2.2.1. Plasma profiles

For plasma density n and temperature T merely entering the computation of the Amjuel-based fractional abundances of excited atoms (Sec. 2.2.3), which are a function of the electron species only [10], $n = n_e$ and $T = T_e$ hold throughout the work.
The normalised poloidal flux coordinate $\psi_{\mathrm{N}} = (\psi - \psi_0)/(\psi_{\mathrm{sep}} - \psi_0)$ is employed, with ψ being the magnetic flux, ψ_0 and ψ_{sep} its value on the magnetic axis (sitting at $(R_0\,;\,Z_0) = (+0.49\,;\,-0.01)$ m) and separatrix, respectively.
A Gaussian shape[1] centred on the magnetic axis ($\psi_{\mathrm{N}} = 0$) is assumed for the core plasma profiles [2], with a peak of $n_e^{\psi_{\mathrm{N}}=0} = 2.6 \times 10^{19}$ m^{-3} and $T_e^{\psi_{\mathrm{N}}=0} = 2.5$ keV for density and

[1]Due to the insensitivity of the result to the core plasma parameters (Sec. 4.2), the actual shape of the core profiles is of minor relevance.

temperature, respectively, as informed by the available experimental measurements. The resulting mathematical formulation hence reads:

$$\begin{aligned} n_e^{\text{core}}(\psi_{\text{N}}) &= n_e^{\psi_{\text{N}}=0} \cdot \exp\left\{-\psi_{\text{N}}^2/2\sigma_n^2\right\} \\ T_e^{\text{core}}(\psi_{\text{N}}) &= T_e^{\psi_{\text{N}}=0} \cdot \exp\left\{-\psi_{\text{N}}^2/2\sigma_T^2\right\} \end{aligned} \tag{1}$$

with $\sigma_n = \left[2\ln\left(n_e^{\psi_{\text{N}}=0}/n_e^{\psi_{\text{N}}=1}\right)\right]^{-1/2}$ and $\sigma_T = \left[2\ln\left(T_e^{\psi_{\text{N}}=0}/T_e^{\psi_{\text{N}}=1}\right)\right]^{-1/2}$ to force the profiles to attain the separatrix values of $n_e^{\psi_{\text{N}}=1} = 1.0 \times 10^{19}$ m^{-3} and $T_e^{\psi_{\text{N}}=1} = 100$ eV (at $\psi_{\text{N}} = 1$), reasonable figures obtained from [11].
Consistently with [11], density and temperature in the edge plasma are assumed to exponentially decay along the radial direction[2], as measured from the plasma magnetic axis. Then:

$$\begin{aligned} n_e^{\text{edge}}(\psi_{\text{N}}, \theta) &= \max\left[n_e^{\psi_{\text{N}}\to\infty}\ ;\ n_e^{\psi_{\text{N}}=1} \cdot \exp\left\{-(\psi_{\text{N}}-1)/\lambda_n^{\psi_{\text{N}}}\right\} \cdot F(\theta)\right] \\ T_e^{\text{edge}}(\psi_{\text{N}}) &= \max\left[T_e^{\psi_{\text{N}}\to\infty}\ ;\ T_e^{\psi_{\text{N}}=1} \cdot \exp\left\{-(\psi_{\text{N}}-1)/\lambda_T^{\psi_{\text{N}}}\right\}\right] \end{aligned} \tag{2}$$

where the decay lengths in the ψ_{N}-space $\lambda_n^{\psi_{\text{N}}}$ and $\lambda_T^{\psi_{\text{N}}}$ are such that $\lambda_n = 7.8$ cm and $\lambda_T = 1.5$ cm in the physical space, coherently with [11]-based estimates. The resulting power decay length for this scenario would thus be $\lambda_q \sim (1/\lambda_n + 3/2\lambda_T)^{-1} = 0.9$ cm [11], of the expected order of magnitude for a limited plasma [12]. The values of $n_e^{\psi_{\text{N}}\to\infty} = 10^{14}$ m^{-3} and $T_e^{\psi_{\text{N}}\to\infty} = 0.1$ eV ($\sim$ room temperature) instead serve the purpose of preventing n_e^{edge} and T_e^{edge} from dropping substantially below the minimum density and temperature allowed by Amjuel fits [10], hence possibly leading to unreasonable extrapolations [13]. The form factor $F(\theta) = 1 + |\theta|/\pi$ confers to n_e^{edge} the dependence on the poloidal angle $\theta \in [-\pi\,;+\pi]$ expected from the 2-point model for an attached plasma [11], such that n_e^{edge} linearly doubles when moving from outer mid-plane (OMP, $\theta = 0$) to the strike point on the wall (SP, $\theta = \pm\pi$). The edge plasma is instead assumed isothermal along the poloidal direction [11].
Core and edge profiles are ultimately merged to give:

$$\begin{aligned} n_e(\psi_{\text{N}}, \theta) &= \begin{cases} n_e^{\text{core}}(\psi_{\text{N}}) \text{ if } 0 \le \psi_{\text{N}} < 1 \\ n_e^{\text{edge}}(\psi_{\text{N}}, \theta) \text{ if } \psi_{\text{N}} \ge 1 \end{cases} \\ T_e(\psi_{\text{N}}) &= \begin{cases} T_e^{\text{core}}(\psi_{\text{N}}) \text{ if } 0 \le \psi_{\text{N}} < 1 \\ T_e^{\text{edge}}(\psi_{\text{N}}) \text{ if } \psi_{\text{N}} \ge 1 \end{cases} \end{aligned} \tag{3}$$

and are depicted in Fig. 4.

[2] In the present scenario, ψ_{N} is chosen as a suitable proxy for the radial direction.

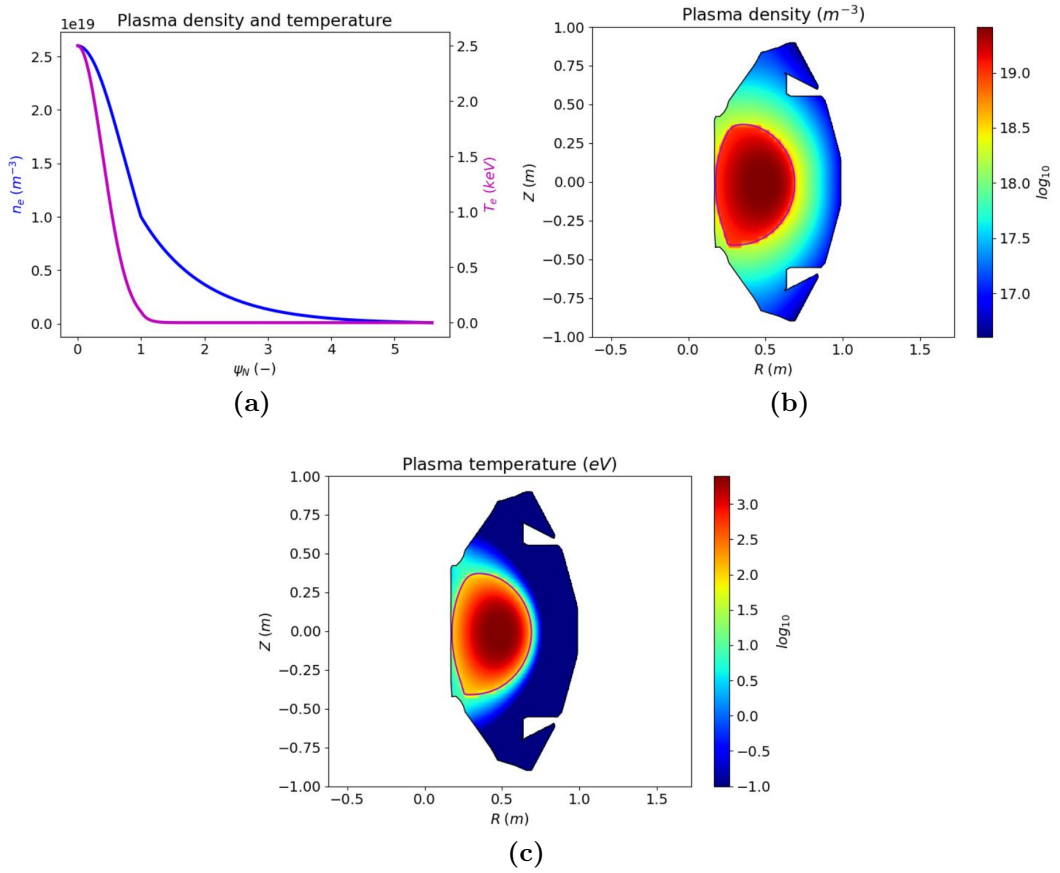

Figure 4: (a) Plasma density n_e (blue, left vertical axis) and temperature T_e (magenta, right vertical axis) as a function of the normalised flux coordinate ψ_{N}. Resulting 2D maps in the poloidal plane for density (b) and temperature (c) in logarithmic scale.

2.2.2. Neutral profiles

An effective neutral density $n_g = n_{\mathrm{D}} + 2n_{\mathrm{D}_2}$ is considered [13], hence not discriminating between atoms D and molecules D_2. Separately accounting for the two species would imply additional degrees of freedom and complexity, and is therefore avoided in the present work. Moreover, ST40 plasmas have been of attached (not detached) nature thus far. In such a regime, discriminating between atomic and molecular mechanisms would presumably give a marginal correction.

The overall neutral density profile is given by the superposition of two contributions:

$$
\begin{aligned}
n_g^{\mathrm{BG}}(\psi_{\mathrm{N}}) &= n_g^{\psi_{\mathrm{N}}=0} + (n_g^{\psi_{\mathrm{N}}\to\infty} - n_g^{\psi_{\mathrm{N}}=0}) \cdot [1 + \exp\{-(\psi_{\mathrm{N}} - 1)/\mu_g\}]^{-1} \\
n_g^{\mathrm{SP}}(R, Z) &= n_{g,0}^{\mathrm{SP}} \cdot \sum_{i=1}^{2} \exp\left\{-(R - R_i)^2/2\sigma_{g,R}^2\right\} \cdot \exp\left\{-(Z - Z_i)^2/2\sigma_{g,Z}^2\right\} \\
\Rightarrow\ n_g(\mathbf{r}) &= n_g(R, Z) = n_g^{\mathrm{BG}}(\psi_{\mathrm{N}}(R, Z)) + n_g^{\mathrm{SP}}(R, Z)
\end{aligned}
\tag{4}
$$

- Depicted in Fig. 5.a, a background (BG) density n_g^{BG} monotonously increasing with ψ_{N}, and such that $\lim_{\psi_{\mathrm{N}}\to\infty} n_g^{\mathrm{BG}}(\psi_{\mathrm{N}}) = n_g^{\psi_{\mathrm{N}}\to\infty}$ away from the separatrix (wall

vicinity), where neutral density gradients vanish. The parameter μ_g quantifies the smoothness of the transition from core to edge plasma around the separatrix.

- Two identical anisotropic Gaussian distributions localised at the two strike points (Sec. 2.1) $(R_1; Z_1) = (+0.177\,;\, +0.2)$ m and $(R_2; Z_2) = (+0.177\,;\, -0.2)$ m, to mimic the recycling-driven enhanced neutral density, and featuring a peak value of $n_{g,0}^{\mathrm{SP}}$. The anisotropic nature is conferred by the standard deviations $\sigma_{g,R} = 0.5$ cm $\ll \sigma_{g,Z} = 5.0$ cm, a reminder of the neutral ionisation mean free path being substantially longer along the Z direction (towards the low-density cold edge plasma) than along the R direction (towards the high-density hot core plasma).

The actual values of the afore-mentioned free parameters are iteratively worked out by subsequent adjustments, and embody the main result of the work (Sec. 4.1). Fig. 5 pictures the resulting profiles.

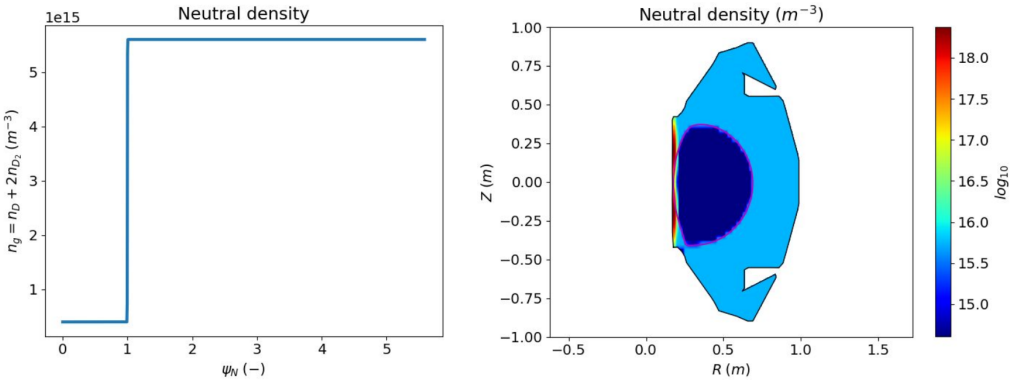

(a) **(b)**

Figure 5: (a) Background neutral density n_g^{BG} as a function of the normalised flux coordinate ψ_{N}. (b) Resulting 2D map in the poloidal plane for $n_g(R,Z) = n_g^{\mathrm{BG}}(\psi_{\mathrm{N}}(R,Z)) + n_g^{\mathrm{SP}}(R,Z)$ in logarithmic scale, with the peaking on the limiter conferred by $n_g^{\mathrm{SP}}(R,Z)$.

2.2.3. D_α emission source

The D_α photons (ν_{32}, Balmer line) are emitted by neutral deuterium atoms D when radiatively de-exciting from the 3rd to the 2nd quantum level[3] (3-2 transition, with 1 being the ground state), according to:

$$\mathrm{D}^*(3) \rightarrow \mathrm{D}^*(2) + \nu_{32} \tag{5}$$

With the plasma profiles commented in Sec. 2.2.1, the Amjuel database[4] [10] allows the computation of the fractional abundance $f_{\mathrm{D}^*(3)}$ $(-)$ (Fig. 6.a) such that $n_{\mathrm{D}^*(3)}(\mathbf{r}) = n_g(\mathbf{r}) \cdot f_{\mathrm{D}^*(3)}(\mathbf{r})$ is the density of neutrals excited in the 3rd quantum level, with the implicit

[3]Splitting of the degenerate quantum levels due to the presence of a strong magnetic field (Paschen-Back effect) can be shown to be a negligible correction in this context.

[4]Specifically, the ratios between the fractional abundances H.12-2.1.5a and H.12-2.1.5tot.

assumptions of n_g comprising all the possible excited states, and of the excitation being driven by neutral-electron interactions[5].

Then, by relying on the transition probability $A_{32} = 4.41 \times 10^7$ s^{-1} for the 3-2 transition [14], the 2D D$_\alpha$ isotropic source S_{D_α} (ph $\cdot$ m^{-3} $\cdot$ s^{-1}) follows (Fig. 6.b):

$$S_\alpha^{\mathrm{2D}}(\mathbf{r}) = A_{32} \cdot n_{\mathrm{D}^*(3)}(\mathbf{r}) \tag{6}$$

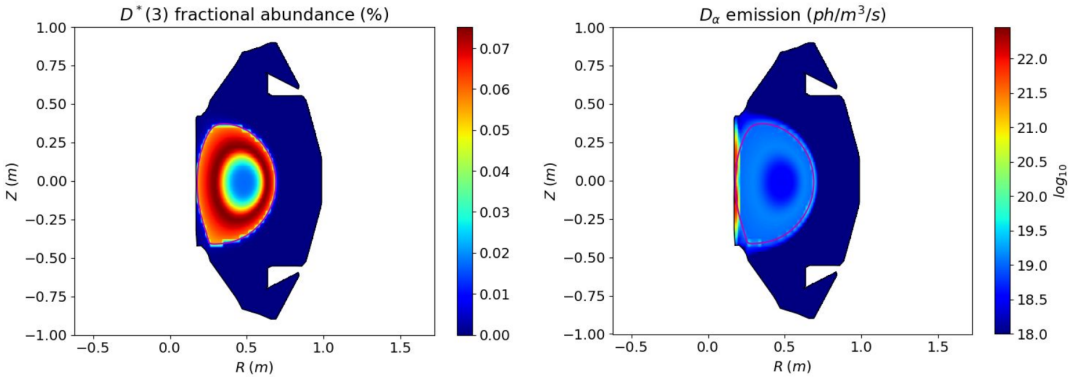

Figure 6: 2D maps in the poloidal plane of (a) fractional abundance $f_{\mathrm{D}^*(3)}(R, Z)$ (%) and (b) isotropic emission source $S_\alpha^{\mathrm{2D}}(R, Z)$, in logarithmic scale.

in a similar manner to the approach adopted by [15] (Eq. 5 therein). The radiation source in (ph $\cdot$ m^{-3} $\cdot$ s^{-1}) is then sampled in CHERAB providing a result expressed in (ph$\cdot$m$^{-2}\cdot$s$^{-1}\cdot$sr^{-1}), and converted to (lux) for experimental comparison according to [16].

3. Novel CHERAB models and algorithms

3.1. 3D periodic piece-wise emission distribution

By default, CHERAB allows the selection among two methods to build 3D emission sources: revolving a 2D source defined in the poloidal plane around the tokamak Z-axis, or considering a source intrinsically 3D.

Via the introduction of a dichotomic function $\mathbb{D}(\phi)$ periodic along the toroidal direction ϕ, a novel 3D emission source model of piece-wise nature is implemented in CHERAB. Because of the experimental emission pattern (Fig. 2.a), such new model is of vital relevance in the present context, but would similarly be of appeal in circumstances as those found in [17] (Fig. 3 therein).

With $N_{\mathrm{LIM}} = 8$ and $\Delta\phi_{\mathrm{LIM}} = 0.23$ rad (= 13 degrees) as per Sec. 2.1, and by defining $\phi_k = 2k\pi/N_{\mathrm{LIM}}$ with $k \in [0\,;\, N_{\mathrm{LIM}} - 1]$, the mathematical expression of the dichotomic

[5]Because of the small neutral density of the present limited scenario (Sec. 4.1), excitation driven by neutral-neutral collisions is neglected.

function and of the corresponding 3D (isotropic) source (schematically represented in Fig. 3) read:

$$\mathbb{D}(\phi) = \begin{cases} 1 \text{ if } \phi_k < \phi < \phi_k + \Delta\phi_{\text{LIM}}/2 \\ 0 \text{ if } \phi_k + \Delta\phi_{\text{LIM}}/2 < \phi < \phi_{k+1} \end{cases} \tag{7}$$

$$\Rightarrow \; S_\alpha^{\text{3D}}(\mathbf{r}, \phi) = \mathbb{D}(\phi) \cdot S_\alpha^{\text{2D}}(\mathbf{r})$$

Particularly, considering the isotropic emission being non-zero only within a region of width $\Delta\phi_{\text{LIM}}/2$ (yellow-blue in Fig. 3) comes from the magnetic shadowing, as discussed in Sec. 2.1. Instead, assuming exactly zero emission in the complementary areas (white in Fig. 3) could be relaxed and some non-zero emission included, but is outside the scope of the present work.
The dichotomic function is then also applied to all the plasma and neutral variables (Sec. 2.2.1 and Sec. 2.2.2, respectively).

3.2. Non-uniform source sampling

Whenever dishomogeneous emission sources are taken into account, sampling (and sample integration afterwards) is carried out along the directions identified by the rays (lines of observation) fired by the camera within the computational scene (reverse ray-tracing) [9][18]. By default and for the sake of simplicity, CHERAB relies upon a uniform sampling (exemplified by the white arrow and dots in Fig. 7.a), i.e. adjacent samples are spaced of a constant quantity Δs (m) - sampling step. Given the strong dishomogeneities featured by the edge plasma and developing over a length in the order of λ_q, the most appropriate sampling step would be such that $\Delta s < \lambda_q$, ideally of a factor ≥ 2. Nevertheless, λ_q attaining values in the millimetres range [19][20] implies a prohibitively small Δs. A new non-uniform sampling algorithm is therefore developed, and schematically shown in magenta in Fig. 7.a. Driving idea is acknowledging the need of fine-sampling exclusively in those regions of space characterised either (1) by elevated emission or (2) by elevated emission gradients, leaving coarse-sampling elsewhere. Mathematically, emphasising such specific areas can be translated in the following criterion:

$$\Delta s^*(\mathbf{r}) = \Delta s_{\max} \cdot \left(\frac{\Delta s_L(\mathbf{r})}{\Delta s_{\max}} \right)^{\frac{w_1 S_\alpha^{\text{2D}}(\mathbf{r})}{\max_{\forall \mathbf{r}} \left[S_\alpha^{\text{2D}}(\mathbf{r}) \right]}} \tag{8}$$

$$\begin{aligned} &\text{with} \;\; \Delta s_L(\mathbf{r}) = \max\left[\Delta s_{\min} \,;\, \min\left[\Delta s_{\max} \,;\, L_{\text{1st}}(\mathbf{r})/w_2 \,;\, L_{\text{2nd}}(\mathbf{r})/w_2\right]\right] \\ &\text{and} \;\; L_{\text{1st}}(\mathbf{r}) = S_\alpha^{\text{2D}}(\mathbf{r}) / |\nabla S_\alpha^{\text{2D}}(\mathbf{r})| \\ &\text{and} \;\; L_{\text{2nd}}(\mathbf{r}) = |\nabla S_\alpha^{\text{2D}}(\mathbf{r})| / \|\mathbf{H}\left[S_\alpha^{\text{2D}}(\mathbf{r})\right]\|_2 \end{aligned} \tag{9}$$

In other words, the non-uniform sampling step $\Delta s^*(\mathbf{r})$ depends on the actual location in space $\mathbf{r}$ via the power law of Eq. 8, graphically represented in Fig. 7.b. If $S_\alpha^{\text{2D}}(\mathbf{r}) = 0$ then $\Delta s^*(\mathbf{r}) = \Delta s_{\max}$ (under user-selection, likewise $\Delta s_{\min}$) and the sampling is the most coarse allowed. Conversely, if $S_\alpha^{\text{2D}}(\mathbf{r}) > 0$ then $\Delta s^*(\mathbf{r})$ would depend on $\Delta s_L(\mathbf{r}) \in [\Delta s_{\min}\,; \Delta s_{\max}]$, with L_{1st} and L_{2nd} (involving the 2-norm $\|\cdot\|_2$ of the Hessian matrix $\mathbf{H}$ [21]) being the characteristic length scales (m) over which the emission $S_\alpha^{\text{2D}}(\mathbf{r})$ and its gradient $\nabla S_\alpha^{\text{2D}}(\mathbf{r})$ vary, respectively, and, hence, must be spatially resolved. The weights w_1 and w_2 $(-)$

are under user-control and put more emphasis (proportionally smaller Δs^*) on the regions where the emission is closest to the maximum and where it varies the most, respectively. The values employed in this work are $w_1 = 45$ and $w_2 = 30$.

Once a satisfactory 2D function $\Delta s^*(\mathbf{r})$ is built in the pre-processing phase by choosing $\Delta s_{\min}$ and $\Delta s_{\max}$ and adjusting w_1 and w_2 (Fig. 7.b), the corresponding 3D version is obtained by a mere revolution around the Z axis (no dependence on ϕ). Whether employing a method likewise Sec. 3.1's would give an advantage despite the enhanced complexity (especially around the periodic discontinuities) is currently dubious and left for future investigation.

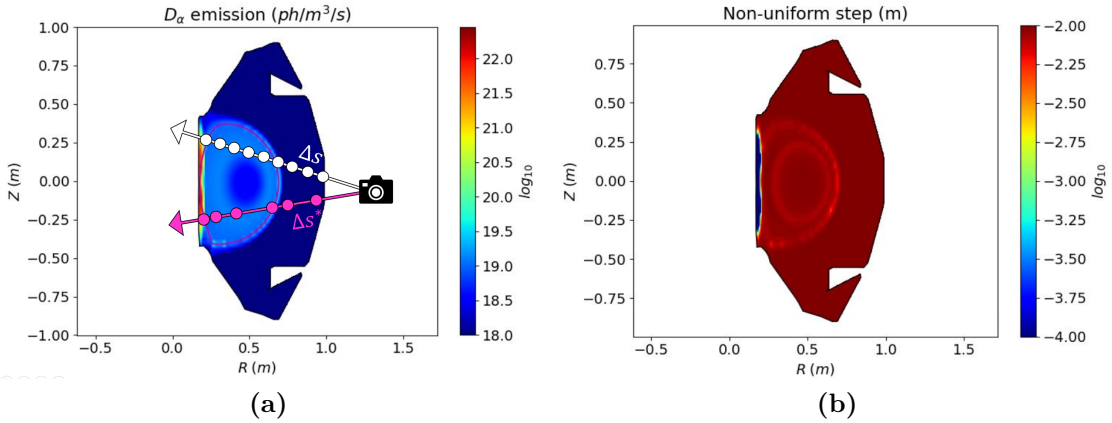

(a) (b)

Figure 7: (a) Cartoon of the uniform (white, default in CHERAB) and non-uniform (magenta, newly-implemented) source sampling along the direction of two representative rays fired by the camera (reverse ray-tracing), overlaid to the emission distribution. The arrows identify the ray direction (observation line), the dots are the samples collected. (b) Map of the newly-implemented non-uniform sampling step $\Delta s^*(R, Z)$ with $\Delta s_{\min} = 10^{-4}$ m, $\Delta s_{\max} = 10^{-2}$ m, $w_1 = 45$, and $w_2 = 30$, as used in the present work.

3.3. Opaque plasma: photon absorption and scattering

Customarily relied upon is the approximation of optically thin plasma [22], which assumes the photons emitted by the plasma to leave the plasma itself unperturbed. In CHERAB this translates into rectilinear ray trajectories the source samples are collected along (Fig. 7.a). However, with neutral deuterium densities foreseen to exceed 10^{21} m^{-3} in partially- and fully-detached regimes [13][23], plasma opaqueness to photon propagation might be non-negligible. Although such densities are far above those achieved in the ST40 shot under consideration, a $\sim 12\%$ variation is already implied when considering plasma opaqueness (Sec. 4.1), which is therefore meritorious of implementation in view of future applications. This is here carried out according to two strategies, differing in terms of complexity and computational cost.

First, the propagation of rays in an opaque environment is directly simulated via a Monte Carlo procedure, and the emission samples collected along the resulting non-rectilinear trajectory (absorption & scattering). At a fundamental level lies the microscopic cross-section $\sigma_{32}^{\text{abs}} \sim 1.2 \times 10^{-14}$ m^2, which regulates the process of absorption of a ν_{32} photon

by the hand of a $D^*(2)$ excited atom. Such parameter can be computed from [24], where (i) spontaneous emission (A-factors of Sec. 2.2.3), (ii) elastic, and (iii) inelastic contributions to the transition are accounted for, with (i) being the dominant and henceforth the only one actually considered here[6]. Downstream the photon absorption, if the resulting $D^*(3)$ atom subsequently meets a radiative 3-2 de-excitation via emission of a ν_{32} photon (44% probability[7]), the original ν_{32} is considered as (isotropically) scattered. Instead, if a radiative 3-1 de-excitation is met by $D^*(3)$ (56% probability), the original ν_{32} is assumed as effectively absorbed[8].
Such processes are summarised below:

$$\begin{aligned} \nu_{32} + D^*(2) &\rightarrow D^*(3) \rightarrow \dots \\ \text{Scattering: } D^*(3) &\rightarrow \nu_{32} + D^*(2) \\ \text{Absorption: } D^*(3) &\rightarrow \nu_{31} + D(1) \end{aligned} \tag{10}$$

and implemented in CHERAB via the Delta-tracking method [27] regulated by the absorption macroscopic cross section $\Sigma_{32}^{\text{abs}}(\mathbf{r}, \phi) = \sigma_{32}^{\text{abs}} \cdot n_{D^*(2)}(\mathbf{r}, \phi)$ (m^{-1}) of Fig. 8 (with $n_{D^*(2)}$ computed from the $D^*(2)$ fractional abundance - Sec. 2.2.3).
Second, in addition to the above-mentioned strategy, a simpler purely-absorbing dynamics in the fashion of [28] is implemented by properly weighting the emission samples collected along rectilinear ray trajectories (linear absorption). By relying on the linear attenuation law along the rectilinear direction of each ray, the intensity I_α ($\text{ph} \cdot \text{m}^{-2} \cdot \text{s}^{-1}$) integrated between two consecutive emission samples ($S_\alpha^{3D}(\mathbf{r}_i, \phi_i)$ and $S_\alpha^{3D}(\mathbf{r}_{i+1}, \phi_{i+1})$) at a distance $\Delta s^*(\mathbf{r}_i)$ (Sec. 3.2) reads[9]:

$$\begin{aligned} I_\alpha^{i \rightarrow i+1} =& 1/2 \cdot \left[S_\alpha^{3D}(\mathbf{r}_i, \phi_i) + S_\alpha^{3D}(\mathbf{r}_{i+1}, \phi_{i+1}) \right] \cdot \Delta s^*(\mathbf{r}_i) \\ & \cdot \exp\left\{ -\Sigma_{32}^{\text{abs}}(\mathbf{r}_i, \phi_i) \cdot \Delta s^*(\mathbf{r}_i) \right\} \end{aligned} \tag{11}$$

where the exponential factor embodies the attenuation. The default CHERAB integration algorithm is recovered by setting $\Sigma_{32}^{\text{abs}}(\mathbf{r}, \phi) = 0$.

[6] Particularly, (iii) can be evaluated via experimentally measured values of [25] (2-1 transition) and conservatively according to Drawin formula of [26] (Eq. 1 and 2 therein for 3-2 and 3-1 transitions).

[7] As dictated by the ratio $A_{32}/(A_{32} + A_{31})$ as a function of the transition probabilities for the 3-2 and 3-1 radiative de-excitation ($A_{31} = 5.58 \times 10^7$ s^{-1}) [14].

[8] The circumstance of ν_{31} being further absorbed by a D(1) atom eventually leading to a re-emission of ν_{32} is outside the scope of the present work, and therefore neglected. Codes capable of self-consistently evolving the photon transport in a plasma background nonetheless exist.

[9] Assuming a proper selection of $\Delta s^*(\mathbf{r})$, the plasma can be considered as homogeneous over the spatial scale defined by the sampling step.

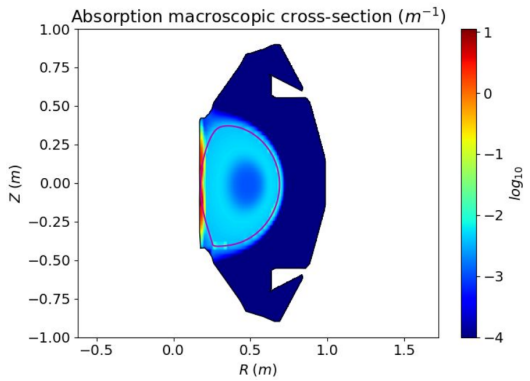

Figure 8: Poloidal distribution of the absorption macroscopic cross section $\Sigma_{32}^{\mathrm{abs}}(R, Z)$.

4. Results

The location, field of view, observation direction, and pixel arrangement (1520 × 1000 uniformly spaced along the horizontal and vertical directions, respectively) of the camera are extracted via the CalCam software [29]. Matching the actual camera pixel distribution is imperative for the synthetic view, to ensure a spatial resolution consistent with the experimental view.
Common to all the simulations, highlights of the settings adopted to build the non-uniform step map are those of Fig. 7.b, with a number of rays (Monte Carlo samples [18][30]) which guarantees a statistical error below 1%. While achieving the same overall accuracy, employing the non-uniform sampling in the present scenario guarantees a >10-fold decrease in the computational cost if compared to equivalent simulations with uniform sampling (with $\Delta s = \Delta s_{\mathrm{min}}$). This advantageously leads to the possibility of relying on PC-class devices, rather than on HPCs. By employing $\Delta s_{\mathrm{max}} = 1 \times 10^{-2}$ m and $\Delta s_{\mathrm{min}} = 1 \times 10^{-4}$ m as in the present study, the computational time with non-uniform sampling approaches ∼0.8 hours, whilst ∼15 hours are required with uniform sampling of step $\Delta s = 1 \times 10^{-4}$ m (8 CPUs in both instances).

4.1. Effect of the different models

A two-fold strategy is employed.
First, a best match with experimental data in the case of optically thin plasma model (baseline) is achieved, both in terms of maximum illuminance (lux) and of integral luminous flux (lm) - computed by integrating the illuminance over the pixel areas. Then, further simulations with the different models are run, with the same plasma and neutral input parameters of the baseline. This allows to gain insight into how different models impact, if at all, the resulting synthetic emission. The results are pictured in Fig. 9. The optically thin plasma baseline case (Fig. 9.b) well matches the experimental view (Fig. 9.a), both from a qualitative and quantitative standpoint. The strong qualitative similarity crucially follows from the exploitation of the novel 3D periodic piece-wise model of Sec. 3.1: the inappropriateness of an axisymmetric source model is clarified by Fig. 9.c. The quantitative agreement is instead justified by the synthetic maximum illuminance (maximum) and integral luminous flux (integral) satisfactorily falling within 2% and 21%

of the experimental data's, respectively. Neutral densities of $n_g^{\psi_N=0} \sim 4.0 \times 10^{14}$ m^{-3} in the core plasma, $n_g^{\psi_N \to \infty} \sim 5.6 \times 10^{15}$ m^{-3} in the far-edge plasma (outer wall vicinity), and $n_{g,0}^{SP} \sim 3.8 \times 10^{18}$ m^{-3} around the strike points are estimated. The other results (from Fig. 9.c to .f) departing from the baseline is therefore to be entirely ascribed to the different models considered. In the respect of Sec. 3.3, the maximum emission obtained in Fig. 9.d by considering rectilinear ray trajectories and attenuating the weight of the emission samples (linear absorption) leads to a $\sim 12\%$ and $\sim 3\%$ reduction in the maximum and integral, respectively. Instead, a mere $\sim 3\%$ and $\sim 1\%$ drop of the maximum and integral can be appreciated in Fig. 9.e when both absorption and scattering are activated and non-rectilinear ray trajectories simulated (absorption & scattering). The mild effects are presumably due to the reduced neutral density ($< 10^{19}$ m^{-3}) characteristic of this limited plasma, in contrast to predictions estimating neutral densities 2 orders of magnitude larger in detached regimes [13][23]. With absorption and scattering heavily depending on such parameter, a marginal importance in this low-neutral-density case is reasonable. For the sake of illustration, Fig. 9.f shows a synthetic view obtained with a 100-fold increase in the microscopic cross-section[10] (absorption & scattering $\times 100$): the corresponding 10-fold reduction in the maximum stresses how plasma opaqueness could substantially impact the predictions.

[10] Increasing the neutral density instead of the cross section would nullify the validity of the assumptions of Sec. 2.2.1 and 2.2.2, as the plasma would enter a detached state and more sophisticated models would be required. The *escamotage* of artificially increasing the cross section is indeed for illustration purposes only.

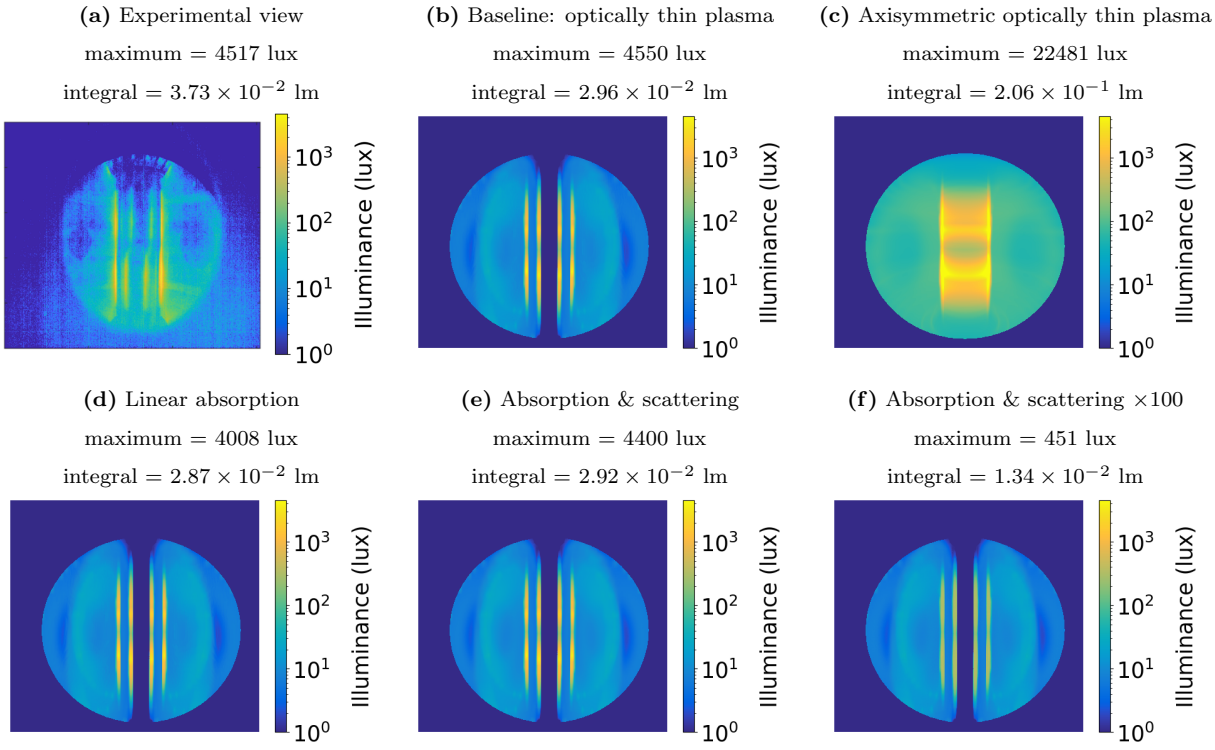

Figure 9: (a) D_α camera experimental view (lux) (as per Fig. 1.b, repeated here for the sake of ease of comparison). (b) Baseline scenario, approximation of optically thin plasma with novel 3D periodic piece-wise emission pattern. (c) Approximation of optically thin plasma with CHERAB default axisymmetric source. (d) Newly-implemented linear absorption. (e) Newly-implemented Delta-tracking-based absorption and scattering, in (f) with ×100 magnification. Free parameters of (b) are employed in each instance. The top end of each logarithmic colorbar matches the maximum illuminance of instance (a).

Second, simulations with the different models are run, with case-specific neutral parameters so that each instance is independently best-matched against experimental data, to understand the sensitivity of the neutral densities (main output) to the particular model adopted. The case-specific parameters are listed in Tab. 1 and the results in Fig. 10, with a satisfactory agreement with the data achieved in each instance: within 2% for the maximum value of the illuminance, and within 21% for the integral luminous flux. No particular neutral parameter stands out as a most influential: by excluding the axisymmetric instance (in qualitative spark contrast with the experiment), $n_g^{\psi_N=0}$, $n_g^{\psi_N\to\infty}$, and $n_{g,0}^{SP}$ are seen to vary up to 15% at most, hence suggesting the robustness of the obtained results with respect to the neutral figures, at least within an uncertainty of 15% (not accounting for other sources of uncertainty, e.g. model uncertainty).

Case	Maximum (lux)	$n_g^{\psi_N=0}$ (m^{-3})	$n_g^{\psi_N\to\infty}$ (m^{-3})	$n_{g,0}^{SP}$ (m^{-3})
Experimental	4517	–	–	–
Optically thin plasma	4550	4.0E+14	5.6E+15	3.8E+18
Axisymmetric thin plasma	4470	1.0E+12	1.0E+13	1.3E+18
Linear absorption	4568	4.6E+14	6.5E+15	4.4E+18
Absorption & scattering	4560	4.1E+14	5.8E+15	3.9E+18

Table 1: Summary of the maximum emission and neutral parameters adopted in the different cases, separately tuned to achieve the best match possible in terms of maximum illuminance and integral luminous flux.

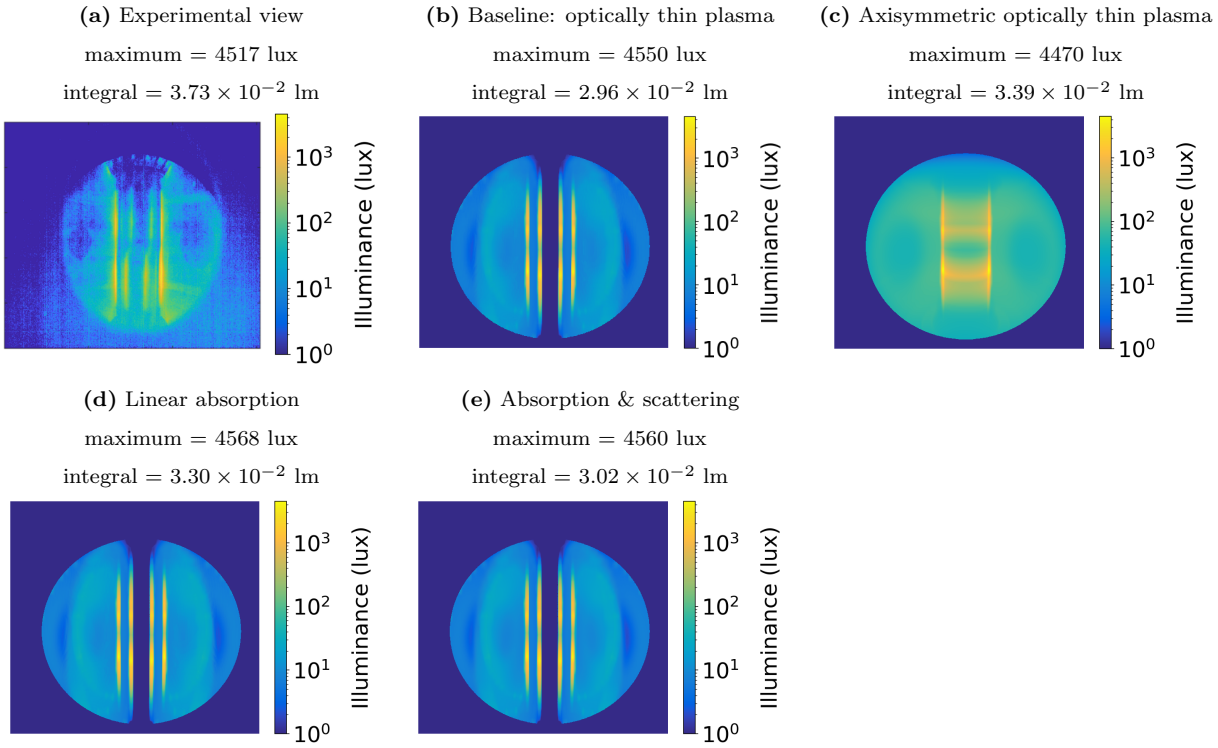

Figure 10: (a) D_α camera experimental view (lux) (as per Fig. 1.b, repeated here for the sake of ease of comparison). (b) Baseline scenario, approximation of optically thin plasma with novel 3D periodic piece-wise emission pattern. (c) Approximation of optically thin plasma with CHERAB default axisymmetric source. (d) Newly-implemented linear absorption. (e) Newly-implemented Delta-tracking-based absorption and scattering. The free parameters are separately tuned in each instance. The top end of each logarithmic colorbar matches the maximum illuminance of instance (a).

4.2. Assessment of robustness to free and uncertain parameters

The present section aims at quantifying the overall sensitivity of the outcome with respect to the parameters involved. By adopting the same settings as per the baseline

simulation of Sec. 4.1 (also in Fig. 11.a), and by changing one parameter at a time of an order of magnitude, the impact on the synthetic view is highlighted. Primary judgement metrics selected are the qualitative agreement to the baseline view, the maximum illuminance (lux), and the integral luminous flux (lm) over the picture.

Fig. 11 shows the results of the study. Minor sensitivity as a function of the core plasma parameters ($\psi_{\mathrm{N}} = 0$, e.g. uncertainty in experimental measurements of Sec. 2.1) is apparent from Fig. 11.b and 11.c, in fact implied by the mild dependence of Amjuel fits on plasma density and temperature [10], at least for the narrow ranges spanned by a limited plasma.

Conversely, edge plasma features at the separatrix ($\psi_{\mathrm{N}} = 1$) do play a substantial role, presumably because of the direct impact on the D_α emission distribution which peaks in the very attached edge plasma, hence characterised by strong dependence of the downstream (at the limiter) quantities on their upstream (at the separatrix) counterparts [11]. Although the values of $T_e^{\psi_{\mathrm{N}}=1}/10 = 10$ eV and $n_e^{\psi_{\mathrm{N}}=1}/10 = 10^{18}$ m^{-3} seemingly lie well outside a reasonable error-bar [2], in-depth specific analyses of the ST40 edge plasma would shed light in this respect, but are outside the scope of the present paper. Then, the farther away from the separatrix, the milder the impact of any changes, as justified by the absence of any appreciable effects by varying the background plasma quantities ($\psi_{\mathrm{N}} \to \infty$), a welcomed result given their primary purely-numerical purpose of preventing accidental divergence of the Amjuel fits (Sec. 2.2.1). Similarly, the actual value of the decay lengths $\lambda_n^{\psi_{\mathrm{N}}}$ and $\lambda_T^{\psi_{\mathrm{N}}}$ (Fig. 11.k and .l, respectively) does not heavily impact the result either.

Because of the direct link to the maximum D_α emission, the peak neutral density on the limiters $n_{g,0}^{\mathrm{SP}}$ has a strong impact on the maximum illuminance and on the integral luminous flux, both scaling almost linearly with such parameter. Sensitivity of the simulations results to $n_{g,0}^{\mathrm{SP}}$, on the one hand, warns the user on the uncertainty of the output but, on the other hand, implies this to be a reliable method to estimate the peak neutral density, which would be instead nullified by a marginal effect of $n_{g,0}^{\mathrm{SP}}$.

Conversely, $n_g^{\psi_{\mathrm{N}}=0}$ and $n_g^{\psi_{\mathrm{N}}\to\infty}$, while not appreciably affecting the maximum illuminance, do show an effect on the integral luminous flux and on the qualitative aspect of the image. In particular, a 10-fold increase in $n_g^{\psi_{\mathrm{N}}=0}$ implies an enhanced background emission and, as a consequence, an increase of the same order on the integral luminous flux with respect to the baseline scenario. In regards to $n_g^{\psi_{\mathrm{N}}\to\infty}$ being increased of a factor 10, a negligible change in the integral luminous flux is found, but accompanied by a substantially different image from a qualitative standpoint, hence no more in agreement with the experimental view.

Recovering a good agreement with experimental data in each of the aforementioned instances has been attempted by re-tuning the remaining parameters, but satisfactory accuracy could not be achieved, hence suggesting the baseline scenario results to be the one most reliable. The overall sensitivity to the neutral densities implies the welcomed feature of this approach to firmly constraining such values, at least within the uncertainties of the present method.

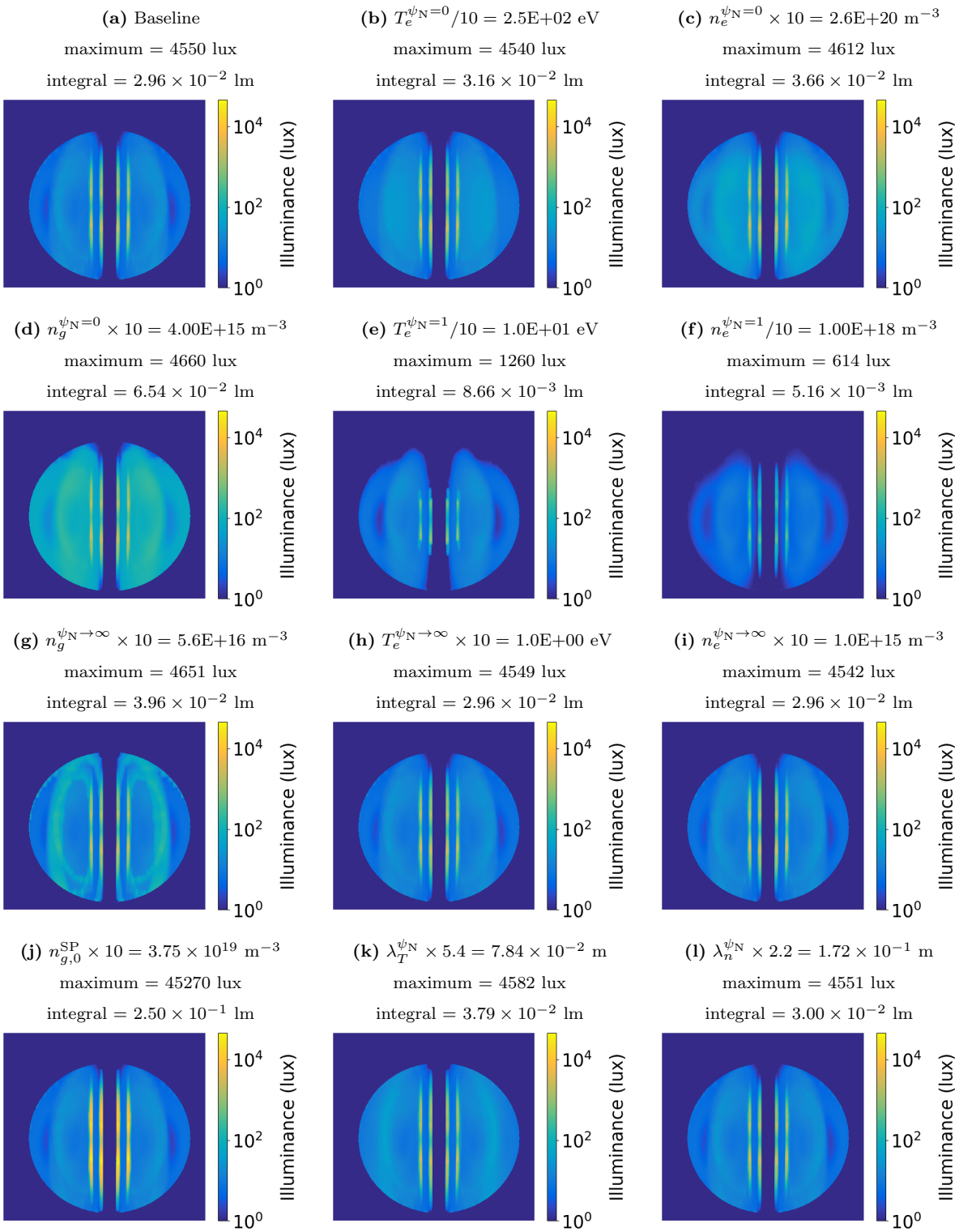

Figure 11: (a) Baseline scenario of Sec. 4.1, then modified by changing: (b) core plasma temperature; (c) core plasma density; (d) core neutral density; (e) separatrix plasma temperature; (f) separatrix plasma density; (g) background neutral density; (h) background plasma temperature; (i) background plasma density; (j) neutral density at strike points; (k) edge plasma temperature decay length; (l) edge plasma density decay length. The top end of each logarithmic colorbar matches the maximum illuminance of instance (a).

5. Conclusions

In the present work, the synthetic 2D view of the D_α camera in Tokamak Energy ST40 device [5] is reconstructed using the CHERAB code [3][4]. The D_α emission model is based on simple analytical models informed by experimental data. A centre-column limited plasma scenario is considered, and the synthetic data compared with the camera's. The emission model accounts for the 3D nature of the source in limited configuration as well as light scattering and absorption.

Satisfactory qualitative and quantitative agreement is achieved with the baseline simulation, which assumes the plasma to be optically thin (transparent) to the radiation emitted therein, by reliance on the novel piece-wise 3D emission model and by tuning the free model parameters. Corresponding values of $\sim 4.0 \times 10^{14}$ m^{-3}, $\sim 5.6 \times 10^{15}$ m^{-3}, and $\sim 3.8 \times 10^{18}$ m^{-3} are estimated for the neutral deuterium density in the core and far-edge plasma, and in the vicinity of the strike points on the centre column, respectively.

Inclusion of the newly-implemented models accounting for D_α absorption and scattering show, on the one hand, minor modifications for the present limited plasma. On the other hand, the illustrative scenario featuring detached-plasma-like neutral characteristics predicts a substantial reduction of the maximum emission, thus cautioning future analyses in such regime of divertor operation.

Inclusion of more sophisticated emission models and possibility of fast scoping out the parameter space in each instance are made possible by reliance on the novel algorithm for non-uniform sampling. Preferentially placing samples in regions of interest implies a corresponding >10-fold reduction in computational cost. Alongside clear benefits computational-time-wise, enhanced ease in the resolution of the maximum emission and the alleviated burden of proving independence of the results on the sampling settings falling on the user [9] are also implied.

In perspective, the flexibility and applicability of the present method will help on improving the analytical models and overall accuracy in view of future applications. Specifically, discriminating between atomic and molecular deuterium, informing the choice of geometrical free parameters via estimates of the neutral mean free path, and relaxing the assumption of zero-emission in between adjacent limiters would be worth including. Moreover, the generality of the novel CHERAB models and algorithms of Sec. 3 allows their application in circumstances where a numerically-computed radiation source is relied upon, e.g. as computed via core and edge plasma transport codes [9].

6. Acknowledgements

The authors acknowledge the support of the Tokamak Energy team at large, for the useful feedbacks and indications. A deep sign of appreciation then goes to T. Looby, with his insightful discussions on the matter of the non-uniform sampling algorithm, which made possible its implementation.

Bibliography

[1] S. DelMedico, O. Barnouin, M. Petra, G. Miley, On aspects of radiation damage in tokamak diagnostics, in: International Conference on Plasma Science, 1995, pp. 221–. doi:10.1109/PLASMA.1995.532798.

[2] M. Sertoli, J. Wood, B. Lomanowski, E. Delabie, M. Gemmel, H. Willet, A. Dnestrowskii, S. Kaye, A. Sladkomedova, O. Marchuk, Making the most of measurements: results from the integrated diagnostic analysis of the ST40 tokamak, 64th Annual Meeting of the APS Division of Plasma Physics (2022).

[3] M. Carr, A. Meakins, A. Baciero, C. Giroud, Cherab documentation.
URL https://cherab.github.io/documentation/index.html

[4] M. Carr, A. Meakins, A. Baciero, M. Bernert, A. Callarelli, A. Field, C. Giroud, J. Harrison, N. Hawkes, S. Henderson, et al., Towards integrated data analysis of divertor diagnostics with ray-tracing, in: 44th EPS Conference on Plasma Physics, European Physical Society, 2017.

[5] P. Thomas, et al., High temperature plasmas in ST40, 64th Annual Meeting of the APS Division of Plasma Physics (2022).

[6] L. Lao, H. S. John, R. Stambaugh, A. Kellman, W. Pfeiffer, Reconstruction of current profile parameters and plasma shapes in tokamaks, Nuclear Fusion 25 (11) (1985) 1611. doi:10.1088/0029-5515/25/11/007.

[7] T. Looby, M. Reinke, A. Wingen, J. Menard, S. Gerhardt, T. Gray, D. Donovan, E. Unterberg, J. Klabacha, M. Messineo, A software package for plasma-facing component analysis and design: The heat flux engineering analysis toolkit (heat), Fusion Science and Technology 78 (1) (2022) 10–27. doi:10.1080/15361055.2021.1951532.

[8] T. Looby, Tokamak 3D Heat Load Investigations Using an Integrated Simulation Framework: HEAT, Ph.D. thesis, University of Tennessee (2022).
URL https://trace.tennessee.edu/utk_graddiss/7095

[9] M. Moscheni, M. Carr, S. Dulla, F. Maviglia, A. Meakins, G. Nallo, F. Subba, R. Zanino, Parametric study of the radiative load distribution on the EU-DEMO first wall due to SPI-mitigated disruptions, Fusion Engineering and Design 172 (2021) 112917. doi:https://doi.org/10.1016/j.fusengdes.2021.112917.

[10] D. Reiter, The data file AMJUEL: Additional Atomic and Molecular Data for EIRENE (2020).
URL http://www.eirene.de/html/amjuel.html

[11] P. Stangeby, The Plasma Boundary of Magnetic Fusion Devices, Series in Plasma Physics and Fluid Dynamics, Taylor & Francis, 2000.
URL https://books.google.co.uk/books?id=qOliQgAACAAJ

[12] M. Kocan, R. Pitts, G. Arnoux, I. Balboa, P. de Vries, R. Dejarnac, I. Furno, R. Goldston, Y. Gribov, J. Horacek, M. Komm, B. Labit, B. LaBombard, C. Lasnier, R. Mitteau, F. Nespoli, D. Pace, R. Panek, P. Stangeby, J. Terry, C. Tsui, P. Vondracek, Impact of a narrow limiter SOL heat flux channel on the ITER first wall panel shaping, Nuclear Fusion 55 (3) (2015) 033019. doi:10.1088/0029-5515/55/3/033019.

[13] M. Moscheni, C. Meineri, M. Wigram, C. Carati, E. D. Marchi, M. Greenwald, P. Innocente, B. LaBombard, F. Subba, H. Wu, R. Zanino, Cross-code comparison of the edge codes SOLPS-ITER, SOLEDGE2D and UEDGE in modelling a low-power scenario in the DTT, Nuclear Fusion 62 (5) (2022) 056009. doi:10.1088/1741-4326/ac42c4.

[14] W. L. Wiese, J. R. Fuhr, Accurate atomic transition probabilities for hydrogen, helium, and lithium, Journal of Physical and Chemical Reference Data 38 (3) (2009) 565–720. doi:10.1063/1.3077727.

[15] R. Dey, M. B. Chowdhuri, J. Ghosh, R. Manchanda, N. Yadava, U. C. Nagora, P. K. Atrey, J. V. Raval, Y. S. Joisa, R. L. Tanna, A. Team, Modeling of the Hα emission from ADITYA tokamak plasmas, Atoms 7 (4) (2019). doi:10.3390/atoms7040095.

[16] J. R. Meyer-Arendt, Radiometry and photometry: Units and conversion factors, Appl. Opt. 7 (10) (1968) 2081–2084. doi:10.1364/AO.7.002081.

[17] A. Huber, S. Brezinsek, A. Kirschner, P. Ström, G. Sergienko, V. Huber, I. Borodkina, D. Douai, S. Jachmich, C. Linsmeier, B. Lomanowski, G. Matthews, P. Mertens, Determination of tungsten sources in the JET-ILW divertor by spectroscopic imaging in the presence of a strong plasma continuum, Nuclear Materials and Energy 18 (2019) 118–124. doi:https://doi.org/10.1016/j.nme.2018.12.009.

[18] M. Moscheni, Modeling the radiative power load on the EU-DEMO PFCs during a mitigated plasma disruption, Master's thesis, Politecnico di Milano (2020).
URL https://www.politesi.polimi.it/handle/10589/153030

[19] T. Eich, A. Leonard, R. Pitts, W. F. et al., Scaling of the tokamak near the scrape-off layer H-mode power width and implications for ITER, Nuclear Fusion 53 (9) (2013) 093031. doi:10.1088/0029-5515/53/9/093031.

[20] T. Eich, P. Manz, R. Goldston, P. Hennequin, P. D. et al., Turbulence driven widening of the near-SOL power width in ASDEX upgrade H-mode discharges, Nuclear Fusion 60 (5) (2020) 056016. doi:10.1088/1741-4326/ab7a66.

[21] S. Salsa, Partial Differential Equations in Action, UNITEXT, Spinger Cham, 2015. doi:https://doi.org/10.1007/978-3-319-15093-2.

[22] J. Freidberg, Plasma Physics and Fusion Energy, Cambridge University Press, 2007.
URL http://dx.doi.org/10.1017/CBO9780511755705

[23] F. Subba, D. Coster, M. Moscheni, M. Siccinio, SOLPS-ITER modeling of divertor scenarios for EU-DEMO, Nuclear Fusion 61 (10) (2021) 106013. doi:10.1088/1741-4326/ac1c85.

[24] O. Axner, J. Gustafsson, N. Omenetto, J. D. Winefordner, Line strengths, A-factors and absorption cross-sections for fine structure lines in multiplets and hyperfine structure components in lines in atomic spectrometry—a user's guide, Spectrochimica Acta Part B: Atomic Spectroscopy 59 (1) (2004) 1–39. doi:https://doi.org/10.1016/j.sab.2003.10.002.

[25] D. Landhuis, L. Matos, S. C. Moss, J. K. Steinberger, K. Vant, L. Willmann, T. J. Greytak, D. Kleppner, Inelastic collision rates of trapped metastable hydrogen, Phys. Rev. A 67 (2003) 022718. doi:10.1103/PhysRevA.67.022718.

[26] Barklem, P. S., Belyaev, A. K., Guitou, M., Feautrier, N., Gadéa, F. X., Spielfiedel, A., On inelastic hydrogen atom collisions in stellar atmospheres, A&A 530 (2011) A94. doi:10.1051/0004-6361/201116745.

[27] J. Rehak, L. Kerby, M. DeHart, R. Slaybaugh, Weighted delta-tracking in scattering media, Nuclear Engineering and Design 342 (2019) 231–239. doi:https://doi.org/10.1016/j.nucengdes.2018.12.006.

[28] V. Sizyuk, A. Hassanein, New proposed iter divertor design using carbon insert on tungsten to mitigate elms and secondary radiation effects on nearby components, Sci. Rep. 12 (2022) 4698. doi:10.1038/s41598-022-08837-2.

[29] S. Scott, H. James, F. Tom, C. Jordan, V. S. Sam, M. Jamie, M. Augustin, N. Emily, G. Christian, S. Mark, W. Alasdair, D. Rhys, Calcam (jul 2022). doi:10.5281/zenodo.6891504.

[30] M. Moscheni, M. Carr, S. Dulla, F. Maviglia, A. Meakins, G. Nallo, F. Subba, R. Zanino, Radiative heat load distribution on the EU-DEMO first wall due to mitigated disruptions, Nuclear Materials and Energy 25 (2020) 100824. doi:https://doi.org/10.1016/j.nme.2020.100824.